Proceedings of the 6th IFAC Symposium on Mechatronic Systems, Zhejiang University, Hangzhou, China, April 10-12, 2013

IFAC MECH2013-0021

Extended Kalman Filtering for Robot Joint Angle Estimation Using MEMS Inertial Sensors

Yizhou Wang * **Wenjie Chen** * **Masayoshi Tomizuka** *

* *Department of Mechanical Engineering, University of California, Berkeley (e-mail: {yzhwang@,wjchen@,tomizuka@me.}berkeley.edu)*

Abstract: The possibility of utilizing low-cost MEMS accelerometers and gyroscopes for accurate joint position estimation of the robot manipulator is investigated in this paper. Cascade Kalman filtering formulation is derived from the robot forward kinematics and the stochastic models of the joint motion sensors. We validate the accuracy of the proposed algorithm via experimentation. We also discuss the effect of the nonlinearity in the kinematic model on two approximation methods - the first-order linearization and the unscented transform.

NOMENCLATURE

θ_i	i-th joint angular position
$\dot{\theta}_i$	i-th joint angular velocity
$\ddot{\theta}_i$	i-th joint angular acceleration
$\delta\theta_i$	i-th joint estimation error angle by gyro integration
ω_i	i-th gyroscope measurement
β_i	i-th gyroscope bias drift
$\boldsymbol{a}_i$	i-th accelerometer measurement
$\mathbb{F}_i$	i-th joint frame
$\mathbb{S}_i$	i-th sensor frame
$\boldsymbol{R}_i^j$	rotation matrix of $\mathbb{F}_i$ with respect to $\mathbb{F}_j$
$\boldsymbol{\omega}_i^j$	angular velocity of link i expressed in $\mathbb{F}_j$
$\boldsymbol{\alpha}_i^j$	angular acceleration of link i expressed in $\mathbb{F}_j$
$\ddot{\boldsymbol{p}}_i^j$	linear acceleration of $\mathbb{F}_i$'s origin expressed in $\mathbb{F}_j$
$(\bullet)_i$	variable related with joint i expressed in $\mathbb{S}_i$
$\boldsymbol{r}_{i-1,i}^i$	vector from $\mathbb{F}_{i-1}$'s origin to $\mathbb{F}_i$'s origin w.r.t $\mathbb{F}_i$
$\boldsymbol{d}_i$	vector from $\mathbb{F}_{i-1}$'s origin to $\mathbb{S}_i$'s origin w.r.t $\mathbb{S}_i$
$\boldsymbol{g}_i$	gravity vector w.r.t $\mathbb{F}_i$

1. INTRODUCTION

The utilization of humanoid robots, such as PR2 (Ackerman [2011]) and NAO (Niemüller et al. [2011]), in households and workspaces can be popularized, or this course might be expedited if their costs are reduced. For these applications, since milimeter order manipulation errors are less likely to cause drastic performance degradation, low-cost microelectromechanical-systems (MEMS) based inertial sensors can be used for revolute joint angle estimations replacing traditional expensive optical encoders. A representative cost comparison has been made in Roan et al. [2012], where fourfold to tenfold cost improvement can be achieved by using inertial sensors.

Other advantages of using inertia sensors are (i) the ease and flexibility of installation, (ii) the reduction of the structural complexity, especially for passive joints, and (iii) the fact that they can work as a redundant sensing system together with existing encoders for safety. The advancement of MEMS technology further enables the increased accuracy and reliability and the decreased price and size of the MEMS sensors.

Prior research has been done on utilizing different combinations of inertial sensors for the purpose of joint angle estimation. Chen and Tomizuka [2012] developed a two-stage sensor fusion algorithm to estimate the load side joint space information. The method, however, was targeting at industrial applications with the sensor configuration of motor encoders and end-effector MEMS accelerometer. In consideration of cost improvement and reduction of structural complexity, Quigley et al. [2010] proposed an extended Kalman filtering scheme by measuring gravity in the joint frame and relating the joint angles with the measurements using rotation matrices. The estimation breaks down when the rotation axis is parallel to the gravity. Roan et al. [2012] developed a complementary filter fusing the angle estimate from the difference between consecutive acceleration vectors and the rate measurement from a uniaxial gyroscope. The singularity configuration can be dealt with by the gyroscope when the accelerometer cannot provide useful information. Cheng and Oelmann [2010] presented a detailed review on four different joint angle estimation methods specifically for the planar arm configuration.

Most of the aforementioned works utilize only the gravity component in the measured acceleration while neglecting the centripetal and centrifugal components. This is likely to affect the estimation accuracy, especially in the situation where the manipulator undergoes fast motions.

In this paper, this problem is tackled by adopting a full kinematic model for the acceleration and the angular rate measurements. An extended Kalman filtering (EKF) method is proposed to estimate joint space variables in robotic manipulators. The measurements are made with low-cost MEMS tri-axial accelerometers and uni-axial gyroscopes, in place of traditional optical encoders. Estimation accuracies are demonstrated by experiments.

The organization of the paper is as follows. In Section 2, some preliminaries are first reviewed, including the mathematical notations, the link relative angular rate and
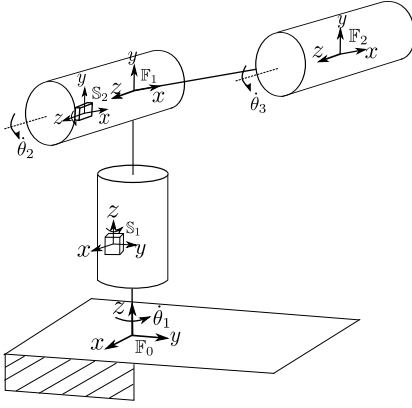
Fig. 1. Definition of the joint frames and the sensor frames.

accelerations as well as the stochastic measurement models of the inertial sensors. Section 3 presents the derivation of an extended Kalman filter for accurate joint angle estimations. In Section 4, the performance of the proposed algorithm is validated by experiments, by comparing the estimates with the high-resolution optical encoder measurements. Section 5 discusses the effect of the measurement model nonlinearity on the estimation accuracy. Finally, the conclusion is drawn in Section 6.

2. PRELIMINARIES

Consider rigidly attaching a coordinate frame $\mathbb{F}_i$ to each link i of the n-DOF robot manipulator at the $i{+}1$th joint rotation axis, with $\mathbb{F}_0$ denoting the world frame. The overall description of the manipulator can be obtained recursively from the kinematic relationship between consecutive links. The Denavit-Hartenberg convention (DH) is adopted to further define $\mathbb{F}_i$.

The proposed algorithm uses a uni-axial gyroscope and a tri-axial accelerometer for each joint. To simplify the description of the position and the orientation of the sensors, assumptions are made that:

(1) the sensor frame $\mathbb{S}_i$ is rigidly attached to link i, $i \in \{1, \cdots, n\}$
(2) the orientation of $\mathbb{S}_i$ is the same as that of $\mathbb{F}_{i-1}$ at the robot home position, $i \in \{1, \cdots, n\}$
(3) the axes of the i-th accelerometer are aligned with those of the sensor frame $\mathbb{S}_i$
(4) the measurement axis of the i-th gyroscope is aligned with the z axis of $\mathbb{S}_i$
(5) the origin of $\mathbb{S}_i$ is the accelerometer measurement point

The proposed joint frames and sensor frames are depicted in Fig. 1.

2.1 Robot forward differential kinematics

This section briefly reviews the relationship between the angular velocities, the angular accelerations and the linear accelerations of consecutive joints as a function of the variables in joint space $\theta_i, \dot{\theta}_i, \ddot{\theta}_i, i \in \{1, ..., n\}$.

It is assumed that each joint provides the mechanical structure with a single DOF, parameterized by the joint variable. For each revolute connection, the relationship can be expressed as follows (detailed in Siciliano et al. [2009]),

$$\boldsymbol{\omega}_i^0 = \boldsymbol{\omega}_{i-1}^0 + \dot{\theta}_i \boldsymbol{z}_{i-1}^0 \tag{1}$$

$$\boldsymbol{\alpha}_i^0 = \boldsymbol{\alpha}_{i-1}^0 + \ddot{\theta}_i \boldsymbol{z}_{i-1}^0 + \dot{\theta}_i \boldsymbol{\omega}_{i-1}^0 \times \boldsymbol{z}_{i-1}^0 \tag{2}$$

$$\ddot{\boldsymbol{p}}_i^0 = \ddot{\boldsymbol{p}}_{i-1}^0 + \boldsymbol{\alpha}_i^0 \times \boldsymbol{r}_{i-1,i}^0 + \boldsymbol{\omega}_i^0 \times (\boldsymbol{\omega}_i^0 \times \boldsymbol{r}_{i-1,i}^0) \tag{3}$$

where $\boldsymbol{\omega}, \boldsymbol{\alpha}$, and $\ddot{\boldsymbol{p}}$ are the angular velocity, the angular acceleration and the linear acceleration respectively. $\boldsymbol{z}_{i-1}^0$ is the z-axis of the frame $\mathbb{F}_{i-1}$ expressed in the frame $\mathbb{F}_0$. In the expressions above, all vectors are expressed with respect to the base frame $\mathbb{F}_0$.

The recursion is computationally more efficient and suitable, if the aforementioned vectors are referred to the current frame $\mathbb{F}_i$. Hence, the following *forward recursions* are derived,

$$\boldsymbol{\omega}_i^i = (\boldsymbol{R}_i^{i-1})^T (\boldsymbol{\omega}_{i-1}^{i-1} + \dot{\theta}_i \boldsymbol{z}_0^0) \tag{4}$$

$$\boldsymbol{\alpha}_i^i = (\boldsymbol{R}_i^{i-1})^T (\boldsymbol{\alpha}_{i-1}^{i-1} + \ddot{\theta}_i \boldsymbol{z}_0^0 + \dot{\theta}_i \boldsymbol{\omega}_{i-1}^{i-1} \times \boldsymbol{z}_0^0) \tag{5}$$

$$\ddot{\boldsymbol{p}}_i^i = (\boldsymbol{R}_i^{i-1})^T \ddot{\boldsymbol{p}}_{i-1}^{i-1} + \boldsymbol{\alpha}_i^i \times \boldsymbol{r}_{i-1,i}^i + \boldsymbol{\omega}_i^i \times (\boldsymbol{\omega}_i^i \times \boldsymbol{r}_{i-1,i}^i) \tag{6}$$

where $\boldsymbol{z}_0^0 = [0\ 0\ 1]^T$, $\boldsymbol{r}_{i-1,i}^i$ is the position vector from the origin of $\mathbb{F}_{i-1}$ to the origin of $\mathbb{F}_i$ expressed in $\mathbb{F}_i$. $\boldsymbol{R}_i^j$ denotes the rotation matrix of $\mathbb{F}_i$ with respect to $\mathbb{F}_j$. From this recursive formula, once the joint variables $\theta_j, \dot{\theta}_j, \ddot{\theta}_j, \forall j \in \{1, ..., i\}$, the velocity $\boldsymbol{\omega}_0^0$ and the acceleration $(\boldsymbol{\alpha}_0^0, \ddot{\boldsymbol{p}}_0^0)$ of the base frame are known, $\boldsymbol{\omega}_i^i, \boldsymbol{\alpha}_i^i$, and $\ddot{\boldsymbol{p}}_i^i$ can be easily computed. The value of $\ddot{\boldsymbol{p}}_0^0$ is conveniently set to $\ddot{\boldsymbol{p}}_0^0 - \boldsymbol{g}_0$, where $\boldsymbol{g}_0$ is the gravity expressed in $\mathbb{F}_0$, so that the rotated gravity is included in $\ddot{\boldsymbol{p}}_i^i$.

2.2 Sensor measurement model

Mathematically, the measurement model of the gyroscope can be written as,

$$\omega_i = \omega_{i,true} + \beta_i + \eta_{wi}$$
$$\dot{\beta}_i = \eta_{\beta i} \tag{7}$$

where the subscript i denotes the joint index, $\omega_{i,true}$ is the true angular velocity, β_i is a drifting bias. The noises η_{wi} and $\eta_{\beta i}$ in the model are usually referred to as the angle random walk (ARW) and the rate random walk (RRW) respectively. Since the z-axes of $\mathbb{S}_i$ and $\mathbb{F}_{i-1}$ are aligned, $\dot{\theta}_i$ can be measured by the i-th gyroscope. Namely, from the z-axis component of Eqn. (4), we have

$$\omega_{i,true} = \omega_{i-1,z}^{i-1} + \dot{\theta}_i \tag{8}$$

where $(\bullet)_z$ denotes the z-axis component of the variable $\bullet$. The accelerometer measurement can be written as,

$$\boldsymbol{a}_i = \ddot{\boldsymbol{p}}_{i,true}^i + \boldsymbol{\eta}_{ai} \tag{9}$$

where $\ddot{\boldsymbol{p}}_{i,true}^i$ represents the actual linear acceleration of the origin of $\mathbb{S}_i$ in $\mathbb{F}_0$ expressed in $\mathbb{S}_i$. $\boldsymbol{\eta}_{ai}$ is the accelerometer measurement noise. We assume that the accelerometer bias is accounted for by the sensor calibration. This is normally valid for constant or slow time-varying bias. The small bias variation will not cause any drift problem like the gyroscope due to the fact that the accelerometer measurement will not be integrated in our algorithm. It is noted that $\boldsymbol{g}_i$, representing the gravity acceleration projected onto $\mathbb{S}_i$, is hidden in the equation as it is already lumped into the first term in the recursive formula

discussed in the forward kinematics.

Utilizing Eqns. (5) and (6), we set the rotation matrix $\boldsymbol{R}_i^{i-1}$ to $\boldsymbol{I}_{3\times3}$ and replace $\boldsymbol{r}_{i-1,i}^i$ by $\boldsymbol{d}_i$, which is the vector from the origin of $\mathbb{F}_{i-1}$ to the origin of $\mathbb{S}_i$ expressed in $\mathbb{S}_i$. Then, the true measurement of the i-th link acceleration can be written explicitly as a function of the angular velocity $\boldsymbol{\omega}_{i-1}^{i-1}$, the angular acceleration $\boldsymbol{\alpha}_{i-1}^{i-1}$, and the linear acceleration $\ddot{\boldsymbol{p}}_{i-1}^{i-1}$ of the previous joint, and the current joint variables $\{\theta_i, \dot{\theta}_i, \ddot{\theta}_i\}$ [1],

$$\ddot{\boldsymbol{p}}_{i,true} = h(\boldsymbol{\omega}_{i-1}^{i-1}, \boldsymbol{\alpha}_{i-1}^{i-1}, \ddot{\boldsymbol{p}}_{i-1}^{i-1}, \theta_i, \dot{\theta}_i, \ddot{\theta}_i, \boldsymbol{d}_i) \qquad (10)$$

The noises $\eta_{wi}, \eta_{\beta i}$, and $\boldsymbol{\eta}_{ai}, i = \{1, \cdots, n\}$, are assumed to be independent, zero-mean, white, and Gaussian distributed, i.e.,

$$E\left\{ \begin{bmatrix} \eta_{wi}(t) \\ \eta_{\beta i}(t) \end{bmatrix} \begin{bmatrix} \eta_{wi}(\tau) \\ \eta_{\beta i}(\tau) \end{bmatrix}^T \right\} = \begin{bmatrix} \sigma_{wi}^2 & 0 \\ 0 & \sigma_{\beta i}^2 \end{bmatrix} \delta(t-\tau)$$

$$E\{\boldsymbol{\eta}_{ai}(t)\boldsymbol{\eta}_{ai}^T(\tau)\} = diag(\sigma_{axi}^2, \sigma_{ayi}^2, \sigma_{azi}^2)\delta(t-\tau) \tag{11}$$

where $\delta(t-\tau)$ is the Dirac-delta function. Using these stochastic models of the gyroscope and the accelerometer measurements, an extended Kalman filtering formulation is derived in the next section.

3. EXTENDED KALMAN FILTERING

This section derives a *cascade* third-order extended Kalman filter for each joint. Namely, during the processing of the i-th EKF, the *a-posteriori* estimates of the states associated with the previous $i-1$ filters are utilized. The computational burden is reduced by this sequential structure because n 3×3 matrices are much easier to process than a $3n\times3n$ matrix (if a single EKF is used to include all joints). However, the estimation accuracy may be compromised in the cascade configuration.

The three states of the i-th filter are defined to be the joint error angle $\delta\theta_i$, the bias β_i, and the joint angular acceleration $\ddot{\theta}_i$. The error angle by integration of the gyroscope measurement is defined as,

$$\delta\theta_i(t) = \int_0^t \omega_i d\tau - \int_0^t \omega_{i-1,z}^{i-1} d\tau - \theta_i(t)$$

$$= \int_0^t (\beta_i + \eta_{wi}) d\tau \tag{12}$$

The filter dynamics for the i-th joint can thus be expressed as,

$$\underbrace{\frac{d}{dt}\begin{bmatrix} \delta\theta_i \\ \beta_i \\ \ddot{\theta}_i \end{bmatrix}}_{\dot{\boldsymbol{x}}(t)} = F \underbrace{\begin{bmatrix} \delta\theta_i \\ \beta_i \\ \ddot{\theta}_i \end{bmatrix}}_{\boldsymbol{x}(t)} + G \underbrace{\begin{bmatrix} \eta_{wi} \\ \eta_{\beta i} \\ \eta_{\gamma i} \end{bmatrix}}_{\boldsymbol{v}(t)} \tag{13}$$

$$\text{where} \quad F = \begin{bmatrix} 0 & 1 & 0 \\ 0 & 0 & 0 \\ 0 & 0 & 0 \end{bmatrix}, \quad G = \begin{bmatrix} 1 & 0 & 0 \\ 0 & 1 & 0 \\ 0 & 0 & 1 \end{bmatrix}$$

and a fictitious noise $\eta_{\gamma i}$ with standard deviation $\sigma_{\gamma i}$ is used to represent the unknown jerk.

---

[1] The expression of the measurement model h can be found in the appendix.

Initialization	$\delta\hat{\theta}_i^-(0) = \delta\theta_{i,o}$ $\qquad \hat{\theta}_i^-(0) = \theta_{i,o}$ $\hat{\beta}_i^-(0) = \beta_{i,o}$ $\qquad\quad \hat{\ddot{\theta}}_i^-(0) = \ddot{\theta}_{i,o}$ $P_i^-(0) = P_{i,o}$
Measurement	measure $\omega_i(k)$ and $\boldsymbol{a}_i(k)$
Known	$\hat{\theta}_j^+(k), \hat{\dot{\theta}}_j^+(k), \hat{\ddot{\theta}}_j^+(k), \quad j = 1, ..., i-1$
Kinematics	compute $\hat{\boldsymbol{\omega}}_{i-1}^{i-1}(k), \hat{\boldsymbol{\alpha}}_{i-1}^{i-1}(k), \hat{\ddot{\boldsymbol{p}}}_{i-1}^{i-1}(k)$ using Eqns (4)–(6)
Filter Gain	$\hat{\dot{\theta}}_i^-(k) = \omega_i(k) - \hat{\omega}_{i-1,z}^{i-1}(k) - \hat{\beta}_i^-(k)$ $H_i(k) = H(\hat{\boldsymbol{\omega}}_{i-1}^{i-1}, \hat{\boldsymbol{\alpha}}_{i-1}^{i-1}, \hat{\ddot{\boldsymbol{p}}}_{i-1}^{i-1}, \hat{\theta}_i^-, \hat{\dot{\theta}}_i^-, \hat{\ddot{\theta}}_i^-, \boldsymbol{d}_i)$ $K_i(k) = P_i^-(k)H_i^T(k)$ $\qquad \cdot\left[H_i(k)P_i^-(k)H_i^T(k) + R_d\right]^{-1}$
Correction	$\begin{bmatrix} \delta\hat{\theta}_i^+(k) \\ \hat{\beta}_i^+(k) \\ \hat{\ddot{\theta}}_i^+(k) \end{bmatrix} = \begin{bmatrix} \delta\hat{\theta}_i^-(k) \\ \hat{\beta}_i^-(k) \\ \hat{\ddot{\theta}}_i^-(k) \end{bmatrix} + K_i(k)\Big[\boldsymbol{a}_i(k)$ $\qquad -h(\hat{\boldsymbol{\omega}}_{i-1}^{i-1}, \hat{\boldsymbol{\alpha}}_{i-1}^{i-1}, \hat{\ddot{\boldsymbol{p}}}_{i-1}^{i-1}, \hat{\theta}_i^-, \hat{\dot{\theta}}_i^-, \hat{\ddot{\theta}}_i^-, \boldsymbol{d}_i)\Big]$ $P_i^+(k) = [I_{3\times3} - K_i(k)H_i(k)]P_i^-(k)$ $\hat{\theta}_i^+(k) = \hat{\theta}_i^-(k) + \delta\hat{\theta}_i^-(k) - \delta\hat{\theta}_i^+(k)$ $\hat{\dot{\theta}}_i^+(k) = \omega_i(k) - \hat{\omega}_{i-1,z}^{i-1}(k) - \hat{\beta}_i^+(k)$
Propagation	$\delta\hat{\theta}_i^-(k+1) = \hat{\beta}_i^+(k)\Delta t$, i.e., reset $\delta\hat{\theta}_i^+(k) = 0$ $\hat{\theta}_i^-(k+1) = \hat{\theta}_i^+(k) + \hat{\dot{\theta}}_i^+(k)\Delta t$ $\hat{\beta}_i^-(k+1) = \hat{\beta}_i^+(k)$ $\hat{\ddot{\theta}}_i^-(k+1) = \hat{\ddot{\theta}}_i^+(k)$ $P_i^-(k+1) = F_d P_i^+(k)F_d^T + G_d Q_d G_d^T$

Table 1. Cascade extended Kalman filtering procedure for the i-th joint angle estimation.

The system matrices and the process noise covariance matrix associated with the discretized system F_d, G_d, Q_d are derived below with the sampling time Δt,

$$\boldsymbol{x}_d(k+1) = F_d \boldsymbol{x}_d(k) + G_d \boldsymbol{v}_d(k)$$

$$F_d = \begin{bmatrix} 1 & \Delta t & 0 \\ 0 & 1 & 0 \\ 0 & 0 & 1 \end{bmatrix}, \quad G_d = \begin{bmatrix} \Delta t & \frac{1}{2}\Delta t^2 & 0 \\ 0 & \Delta t & 0 \\ 0 & 0 & \Delta t \end{bmatrix}$$

$$Q_d = \begin{bmatrix} \sigma_{wi}^2\Delta t + \frac{1}{3}\sigma_{\beta i}^2\Delta t^3 & \frac{1}{2}\sigma_{\beta i}^2\Delta t^2 & 0 \\ \frac{1}{2}\sigma_{\beta i}^2\Delta t^2 & \sigma_{\beta i}^2\Delta t & 0 \\ 0 & 0 & \sigma_{\gamma i}^2\Delta t \end{bmatrix} \tag{14}$$

The measurement model of the Kalman filter, which is the composition of Eqns. (9) and (10), is a nonlinear function of the state variables

$$\boldsymbol{a}_i = h(\boldsymbol{\omega}_{i-1}^{i-1}, \boldsymbol{\alpha}_{i-1}^{i-1}, \ddot{\boldsymbol{p}}_{i-1}^{i-1}, \theta_i, \dot{\theta}_i, \ddot{\theta}_i, \boldsymbol{d}_i) + \boldsymbol{\eta}_{ai} \tag{15}$$

The Jacobian matrix of h with respect to the states, $H = \nabla h$, when evaluated at the *a-priori* estimate of the

current filter state $\{\hat{\theta}_i^-, \hat{\dot{\theta}}_i^-, \hat{\ddot{\theta}}_i^-\}$, is written as [2],

$$H = H(\hat{\boldsymbol{\omega}}_{i-1}^{i-1}, \hat{\boldsymbol{\alpha}}_{i-1}^{i-1}, \hat{\ddot{\boldsymbol{p}}}_{i-1}^{i-1}, \hat{\theta}_i^-, \hat{\dot{\theta}}_i^-, \hat{\ddot{\theta}}_i^-, \boldsymbol{d}_i) \qquad (16)$$

where $\hat{\boldsymbol{\omega}}_{i-1}^{i-1}, \hat{\boldsymbol{\alpha}}_{i-1}^{i-1}, \hat{\ddot{\boldsymbol{p}}}_{i-1}^{i-1}$ are obtained from the *a-posteriori* estimates of the previous joint variables $\{\hat{\theta}_j^+, \hat{\dot{\theta}}_j^+, \hat{\ddot{\theta}}_j^+ \mid j = 1, \ldots, i-1\}$. The measurement noise covariance matrix in the discrete-time formulation is

$$R_d = R/\Delta t = diag(\sigma_{axi}^2, \sigma_{ayi}^2, \sigma_{azi}^2)/\Delta t \qquad (17)$$

The detailed procedure of the proposed extended Kalman filter for the i-th joint is summarized in Tab. 1. By incorporating the acceleration information, the proposed algorithm is drift-free, as long as the axis of rotation is not always parallel to the gravity. Also, the algorithm is expected to work for general motions, due to the inclusion of the motion acceleration in the model.

4. EXPERIMENTAL RESULTS

The performance of the proposed extended Kalman filtering method is evaluated via experiments. Figure 2(a) shows the 9-DOF IMU developed in the Mechanical Systems Control Laboratory at UC Berkeley. It has an Arduino Pro Mini microprocessor and a Sparkfun 9-DOF sensor stick (ADXL345 accelerometer, HMC5843 magnetometer, ITG-3200 gyroscope) onboard. In the experiments, the tri-axial accelerometers and only one axis of each gyroscope are actually utilized. The sampling frequency is set to 75Hz due to hardware limitation since the clock rate of the processor is only 8MHz. The raw data is transfered to the external computer and recorded. The joint angle estimates are calculated offline using the same sampling rate of 75 Hz.

During experiments, two IMUs are rigidly attached to the red and blue gimbals of the Quanser 3-DOF gyroscope in Fig.2(b), which serve as two consecutive revolute joints and are moved manually in arbitrary trajectories. The outer rectangular gimbal is fixed. The estimation accuracy is evaluated by comparing the estimates with the measurements from 5000 pulses per revolution quadrature encoders.

Two other estimation schemes are also performed and compared. One is simply from integrating the gyroscope measurements (abbr. GYRO), which suffers from bias drift. The other (abbr. ACC) is to treat the accelerometer measurements as the gravity vector related with the joint angle as

$$\begin{bmatrix} g_{i,x} \\ g_{i,y} \\ g_{i,z} \end{bmatrix} = \begin{bmatrix} \cos\theta_i & -\sin\theta_i & 0 \\ \sin\theta_i & \cos\theta_i & 0 \\ 0 & 0 & 1 \end{bmatrix} \begin{bmatrix} g_{i-1,x} \\ g_{i-1,y} \\ g_{i-1,z} \end{bmatrix} \qquad (18)$$

where $g_{i,\bullet}$ denotes the gravity component on the $\bullet$-axis of the frame $\mathbb{F}_i$. By doing this, it is assumed that the motion acceleration is negligible. The above equation provides two transcendental equations in θ_i which can be solved for the joint angle as follows

$$\theta_i = \text{atan2}(g_{i,y}g_{i-1,x} - g_{i,x}g_{i-1,y}, \ g_{i,x}g_{i-1,x} + g_{i,y}g_{i-1,y}) \qquad (19)$$

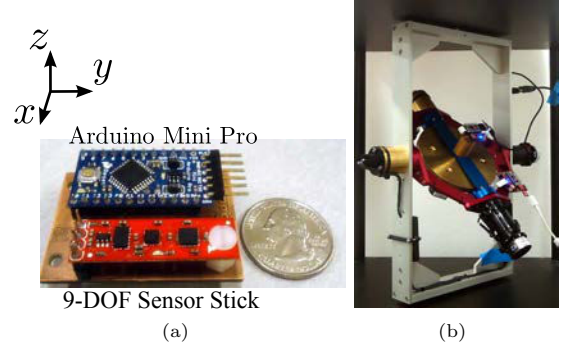[2] The expression of the Jacobian matrix H can be found in the appendix.

Fig. 2. (a) The 9-DOF inertial measurement unit and (b) The quanser 3-DOF gyroscope (size: $0.7m \times 0.5m \times 0.5m$).
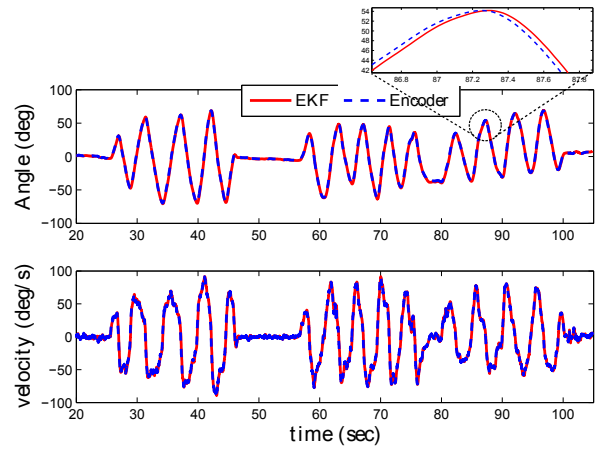

Fig. 3. The EKF estimates of the joint angle position and velocity of the first joint compared with the encoder measurements
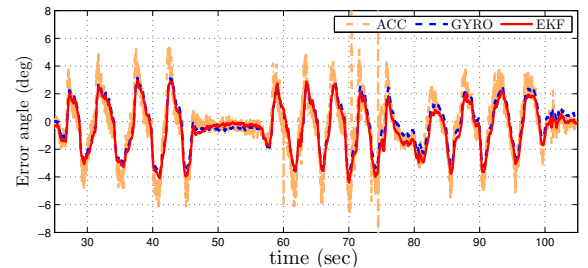

Fig. 4. First joint estimation errors from various methods. The RMS error of the EKF is 1.52°

Figure 3 and 5 show that the EKF estimates of the joint angle position and velocity follow the encoder measurements very closely. Some delays can be observed in the zoom-in plots. The estimation errors are plotted in Fig. 4 and 6. The RMS errors and peak errors are tabulated for various methods in Tab.2.

As expected, the ACC estimates tend to be noisy and their accuracy is sensitive to how well the slow motion assumption is justified. On the other hand, the GYRO estimates are accurate for a short-time duration (Joint 1) but their drifts are accumulated and cannot be corrected (Joint 2).
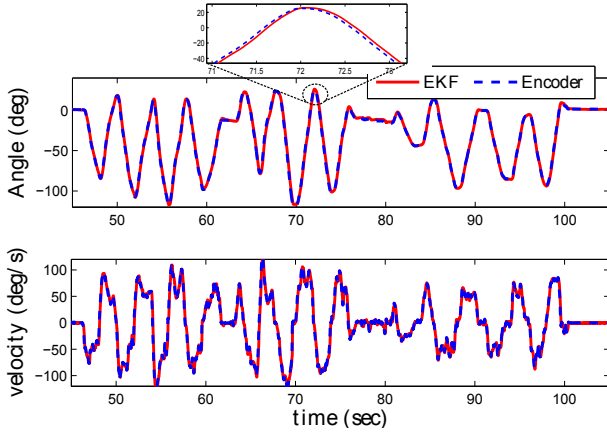
Fig. 5. The EKF estimates of the angle position and velocity of the second joint compared with the encoder measurements
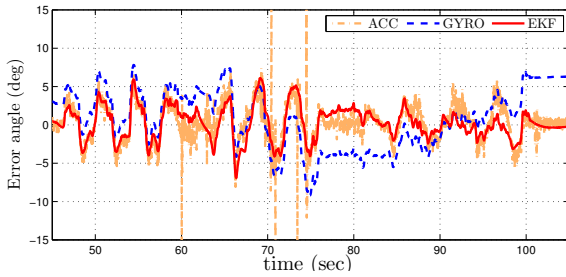

Fig. 6. Second joint estimation errors from various methods. The RMS error of the EKF is 1.66°

	Method	rms error [°]	peak error [°]
Joint 1	EKF	1.52	4.41
	GYRO	1.45	4.04
	ACC	1.88	19.45
Joint 2	EKF	1.66	6.93
	GYRO	3.14	9.21
	ACC	2.16	45.22

Table 2. Estimation accuracy

5. DISCUSSION

It is well known that the EKF algorithm only provides an approximation to optimal nonlinear system state estimation. Namely, the state distribution is approximated by a Gaussian random variable, which is propagated through the first-order linearization of the nonlinear system. Therefore, the approximated posterior mean and covariance agree with the true ones only up to the first order. It is natural to ask how well the EKF deals with the nonlinear measurement model in this application. Do alternative forms of Kalman filter, such as the unscented Kalman filter, likely improve the estimation accuracies?

Julier and Uhlmann [1997] proposed the unscented transform (UT) and rigorously proved that it preserves the posterior mean and covariance up to the second order. However, it is *not* guaranteed that the conditional expectation of a random variable, conditioned on the realized value of a nonlinear measurement and calculated from the unscented transform, is more accurate than that from the first-order linearization (FOL). We demonstrate this for

our application using the simulated distribution of the random state variable $\boldsymbol{X}$ and the measurement output $\boldsymbol{Y}$ at one time step.

5.1 Accuracy of the approximated posterior mean and covariance (a-priori estimate of the output in KF context)

We consider a three-dimensional Gaussian random variable $\boldsymbol{X} = [\theta, \dot{\theta}, \ddot{\theta}]^T$ with mean $\hat{\boldsymbol{x}} = [\hat{\theta}, \hat{\dot{\theta}}, \hat{\ddot{\theta}}] = \boldsymbol{0}$ and covariance $\boldsymbol{\Lambda_{xx}} = \mathrm{diag}(0.001, 0.001, 0.001)$ (SI units). The measurement $\boldsymbol{Y}$, which is a nonlinear function of $\boldsymbol{X}$, is given by,

$$\boldsymbol{Y} = h(\boldsymbol{\omega}, \boldsymbol{\alpha}, \ddot{\boldsymbol{p}}, \theta, \dot{\theta}, \ddot{\theta}, \boldsymbol{d}) \qquad (20)$$

where $\boldsymbol{\omega} = [0, 1.2498, 0]^T$ (rad/sec), $\boldsymbol{\alpha} = [0, -0.2279, 0]^T$ (rad/sec^2), $\ddot{\boldsymbol{p}} = [-6.6696, 0, -7.2059]^T$ (m/sec^2), $\boldsymbol{d} = [-0.029, 0.003, 0.051]^T$ (m) which are from the real data. To see the effect of the nonlinearity only, we assume no measurement noise in $\boldsymbol{Y}$ for simplicity. In order to evaluate the accuracies of the posterior mean and covariance, $N = 10000$ samples of $\boldsymbol{X}$ are generated. They are then propagated through h to obtain the distribution of $\boldsymbol{Y}$.

The first-order linearization and the unscented transform are utilized to approximate the posterior mean and covariance. The actual sample mean and covariance are calculated by,

$$\hat{\boldsymbol{y}} = \frac{1}{N} \sum_{i=1}^{N} \boldsymbol{y}_i \qquad (21)$$

$$\boldsymbol{\Lambda_{yy}} = \frac{1}{N-1} \sum_{i=1}^{N} (\boldsymbol{y}_i - \hat{\boldsymbol{y}})(\boldsymbol{y}_i - \hat{\boldsymbol{y}})^T \qquad (22)$$

The first-order linearization leads to (Welch and Bishop [1995]),

$$\hat{\boldsymbol{y}}^{FOL} = h(\boldsymbol{\omega}, \boldsymbol{\alpha}, \ddot{\boldsymbol{p}}, \hat{\theta}, \hat{\dot{\theta}}, \hat{\ddot{\theta}}, \boldsymbol{d})$$
$$\boldsymbol{\Lambda_{yy}}^{FOL} = H\boldsymbol{\Lambda_{xx}}H^T \qquad (23)$$
$$\boldsymbol{\Lambda_{xy}}^{FOL} = \boldsymbol{\Lambda_{xx}}H^T$$

where $H = H(\boldsymbol{\omega}, \boldsymbol{\alpha}, \ddot{\boldsymbol{p}}, \hat{\theta}, \hat{\dot{\theta}}, \hat{\ddot{\theta}}, \boldsymbol{d})$ is the Jacobian of h with respect to the states. The computations of $\hat{\boldsymbol{y}}^{UT}$, $\boldsymbol{\Lambda_{yy}}^{UT}$, and $\boldsymbol{\Lambda_{xy}}^{UT}$ are detailed in Wan and Van Der Merwe [2000]. Figure 7 compares $\hat{\boldsymbol{y}}^{FOL}$ and $\hat{\boldsymbol{y}}^{UT}$ with $\hat{\boldsymbol{y}}$, plotted with the parabolic distribution of $\boldsymbol{Y}$. As expected, $\hat{\boldsymbol{y}}^{UT}$ approximates $\hat{\boldsymbol{y}}$ more accurately than $\hat{\boldsymbol{y}}^{FOL}$. Figure 8 compares the three covariance ellipsoids centered at the corresponding means. Any point $\boldsymbol{v}$ on each ellipsoid satisfies,

$$(\boldsymbol{v} - \hat{\boldsymbol{y}}^{(\bullet)})^T \boldsymbol{\Lambda_{yy}}^{(\bullet)-1} (\boldsymbol{v} - \hat{\boldsymbol{y}}^{(\bullet)}) = 1 \qquad (24)$$

with the corresponding mean and covariance where ($\bullet$) is UT or FOL. It can be seen that $\boldsymbol{\Lambda_{yy}}^{UT}$ also has better accuracy than $\boldsymbol{\Lambda_{yy}}^{FOL}$, which is a much thinner ellipsoid. In fact, as seen in Fig. 9, $\boldsymbol{\Lambda_{yy}}^{FOL}$ is tangent to the distribution of $\boldsymbol{Y}$, projected on a_x-a_y plane. On the other hand, $\boldsymbol{\Lambda_{yy}}^{UT}$ better captures the parabolic shape of the distribution of $\boldsymbol{Y}$ open in the $+a_x$ direction, while $\boldsymbol{\Lambda_{yy}}^{FOL}$ fails.

5.2 Accuracy of the conditional expectation (a-posteriori correction of the state)

The Kalman filter is derived based on the conditional expectation result. Namely, given two jointly Gaussian
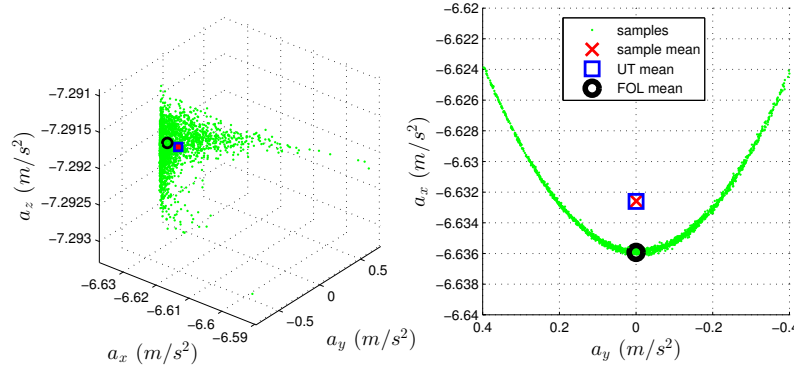
Fig. 7. The UT approximates the posterior mean through a nonlinear transformation more accurately than the FOL.
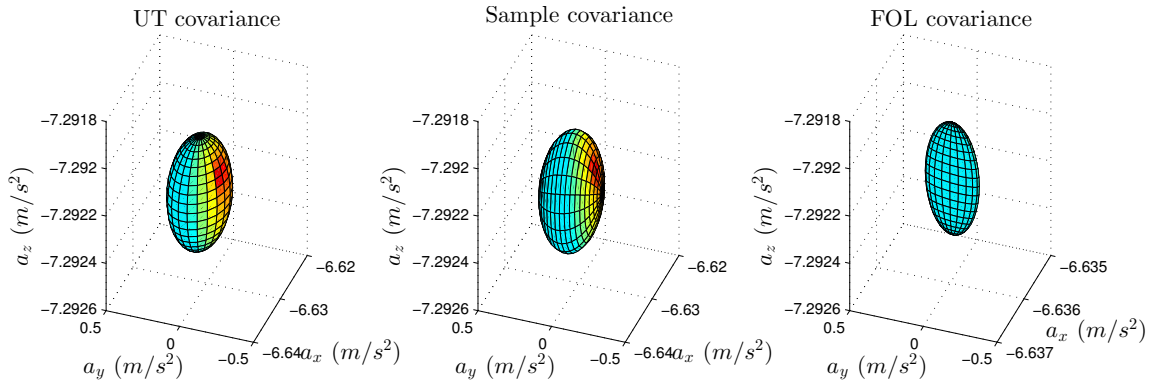

Fig. 8. The UT approximates the posterior covariance through a nonlinear transformation more accurately than the FOL.
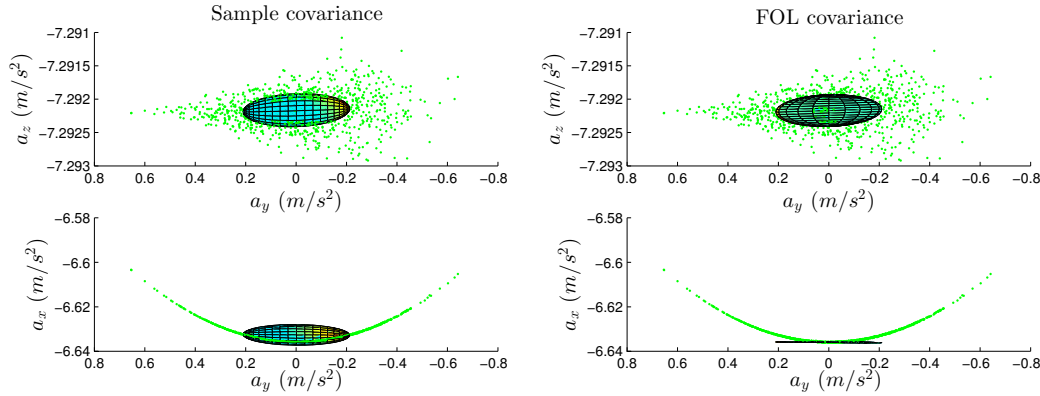

Fig. 9. Detailed comparison between the FOL-predicted and the sample posterior covariances. The UT predicted posterior covariance is not plotted because it looks very similar to the sample covariance. The FOL is not able to capture the parabolic shape of the distribution.

random variables $\boldsymbol{X}$ and $\boldsymbol{Y}$, the conditional mean $\hat{\boldsymbol{X}}|_{\boldsymbol{y}}$ of $\boldsymbol{X}$, conditioned on the realized value of $\boldsymbol{Y}$, is the best estimator of $\boldsymbol{X}$ in the sense of least squares. The computation of $\hat{\boldsymbol{X}}|_{\boldsymbol{y}}$ explicitly depends on $\hat{\boldsymbol{y}}$, $\boldsymbol{\Lambda_{yy}}$, and the cross covariance $\boldsymbol{\Lambda_{xy}}$ as

$$\hat{\boldsymbol{X}}|_{\boldsymbol{y}} = \hat{\boldsymbol{x}} + \boldsymbol{\Lambda_{xy}}\boldsymbol{\Lambda_{yy}^{-1}}(\boldsymbol{y} - \hat{\boldsymbol{y}}) \qquad (25)$$

When $\boldsymbol{Y}$ is non-Gaussian due to the nonlinear measurement model, as we already see the advantage of the unscented transform in the previous section, we expect better accuracy of the approximated conditional mean from the UT than the FOL. However, this is not generally true, as illustrated by the following simulation results.

To estimate an unknown sample of $\boldsymbol{X}$, of which the mean and covariance are known a-priori, we calculate the conditional mean, denoted as $\hat{\boldsymbol{X}}_i^{FOL}|_{\boldsymbol{y}_i}$ and $\hat{\boldsymbol{X}}_i^{UT}|_{\boldsymbol{y}_i}$ using Eqn. (25) with $\hat{\boldsymbol{y}}$, $\boldsymbol{\Lambda_{yy}}$, and $\boldsymbol{\Lambda_{xy}}$ approximated by the first-order linearization and UT respectively. We compare $\hat{\boldsymbol{X}}_i^{FOL}|_{\boldsymbol{y}_i}$, $\hat{\boldsymbol{X}}_i^{UT}|_{\boldsymbol{y}_i}$ with $\boldsymbol{x}_i$ for the following four cases, with all $\boldsymbol{\Lambda_{xx}} = \text{diag}(0.001, 0.001, 0.001)$. The residuals $(\hat{\boldsymbol{X}}_i^{(\bullet)}|_{\boldsymbol{y}_i} - \boldsymbol{x}_i)$ are plotted in Fig. 10 through Fig. 13.

(1) $\hat{\boldsymbol{x}} = [0, \ 0, \ 0]^T$ (Fig. 10)

The FOL causes errors in $\dot{\theta}$ and $\ddot{\theta}$ dimensions while the UT causes small errors in $\dot{\theta}$ dimension.

(2) $\hat{\boldsymbol{x}} = [\pi/2,\ 0,\ 0]^T$ (Fig. 11)

The FOL causes errors in $\dot{\theta}$ and $\ddot{\theta}$ dimensions while the UT causes errors in θ dimension.

(3) $\hat{\boldsymbol{x}} = [0,\ 0.5,\ 0]^T$ (Fig. 12)

The FOL causes errors in $\ddot{\theta}$ dimension and small errors in θ dimension while the UT causes errors in $\dot{\theta}$ dimension.

(4) $\hat{\boldsymbol{x}} = [\pi/2,\ 0.3,\ 0.3]^T$ (Fig. 13)

The FOL causes errors in $\ddot{\theta}$ dimension and small errors in θ dimension while the UT causes errors in θ and $\dot{\theta}$ dimensions.

It should be noted that the accuracy is sensitive to the numerical values that we choose for the parameters. However, these four cases provide the observations that the estimation performance by these two approximations (FOL and UT) is controversial, i.e., there is no guarantee that one would always perform better than the other. The choice of the approximation method would reside in the nature of the application. In this application of estimating the joint angle θ, the FOL is likely to perform better than the UT (as illustrated by the above four cases). Thus, the EKF method is chosen for the purpose of this work.

6. CONCLUSION

This paper presented a cascade extended Kalman filtering method for robotic joint angle estimation. The filter was derived from the robotic forward kinematics and the stochastic model of the MEMS inertial sensors. Via experimentation, the estimation errors of the proposed algorithm were shown to be within around $2°$ which is unlikely to drastically degrade the performance of humanoid robots. Future works include the investigation of the real-time implementation on robots such as PR2, and the development of a systematic way for sensor alignment and calibration.

ACKNOWLEDGEMENTS

REFERENCES

Ackerman. Willow garages introduces pr2 se, half the arms at half the price, 2011. Available: http://spectrum.ieee.org/automaton/robotics/robotics-software/willow-garage-pr2-se-now-available-half-the-arms-at-half-the-price.

W. Chen and M. Tomizuka. Load side state estimation in robot with joint elasticity. In *Advanced Intelligent Mechatronics 2012, IEEE/ASME International Conference on*, pages 598–603, 2012.

P. Cheng and B. Oelmann. Joint-angle measurement using accelerometers and gyroscopesa survey. *Instrumentation and Measurement, IEEE Transactions on*, 59(2):404–414, 2010.

S.J. Julier and J.K. Uhlmann. A new extension of the kalman filter to nonlinear systems. In *Int. Symp. Aerospace/Defense Sensing, Simul. and Controls*, volume 3, page 26. Spie Bellingham, WA, 1997.

Tim Niemüller, Alexander Ferrein, Gerhard Eckel, David Pirro, Patrick Podbregar, Tobias Kellner, Christof Rath, and Gerald Steinbauer. Providing ground-truth data for the nao robot platform. *RoboCup 2010: Robot Soccer World Cup XIV*, pages 133–144, 2011.

M. Quigley, R. Brewer, S.P. Soundararaj, V. Pradeep, Q. Le, and A.Y. Ng. Low-cost accelerometers for robotic manipulator perception. In *Intelligent Robots and Systems (IROS), 2010 IEEE/RSJ International Conference on*, pages 6168–6174, 2010.

P. Roan, N. Deshpande, Y. Wang, and B Pitzer. Manipulator state estimation with low-cost accelerometers and gyroscopes. In *Intelligent Robots and Systems (IROS), 2012 IEEE/RSJ International Conference on*, 2012.

B. Siciliano, L. Sciavicco, and L. Villani. *Robotics: modelling, planning and control.* Springer Verlag, 2009.

E.A. Wan and R. Van Der Merwe. The unscented kalman filter for nonlinear estimation. In *Adaptive Systems for Signal Processing, Communications, and Control Symposium 2000. AS-SPCC. The IEEE 2000*, pages 153–158, 2000.

G. Welch and G. Bishop. An introduction to the kalman filter. *University of North Carolina at Chapel Hill, Chapel Hill, NC*, 7(1), 1995.

Appendix A. LONG EXPRESSIONS

The measurement model h and its Jacobian H are given as follows,

$$\ddot{\boldsymbol{p}}_{true} = h(\boldsymbol{\omega}, \boldsymbol{\alpha}, \ddot{\boldsymbol{p}}, \theta, \dot{\theta}, \ddot{\theta}, \boldsymbol{d})$$
$$= [\ddot{p}_x\ \ddot{p}_y\ \ddot{p}_z]^T \tag{A.1}$$

$$\begin{aligned}
\ddot{p}_x =& -\boldsymbol{\alpha}_z \boldsymbol{d}_y + \boldsymbol{\alpha}_y ci\boldsymbol{d}_z + ci\ddot{\boldsymbol{p}}_x - \boldsymbol{\alpha}_x \boldsymbol{d}_z si + \ddot{\boldsymbol{p}}_y si - ci\boldsymbol{d}_y si\boldsymbol{\omega}_x^2 - \boldsymbol{d}_x si^2\boldsymbol{\omega}_x^2 \\
& + ci^2\boldsymbol{d}_y\boldsymbol{\omega}_x\boldsymbol{\omega}_y + 2ci\boldsymbol{d}_x si\boldsymbol{\omega}_x\boldsymbol{\omega}_y - \boldsymbol{d}_y si^2\boldsymbol{\omega}_x\boldsymbol{\omega}_y - ci^2\boldsymbol{d}_x\boldsymbol{\omega}_y^2 + ci\boldsymbol{d}_y si\boldsymbol{\omega}_y^2 \\
& + ci\boldsymbol{d}_z\boldsymbol{\omega}_x\boldsymbol{\omega}_z + \boldsymbol{d}_z si\boldsymbol{\omega}_y\boldsymbol{\omega}_z - \boldsymbol{d}_x\boldsymbol{\omega}_z^2 - \boldsymbol{d}_y\ddot{\theta} - 2\boldsymbol{d}_x\boldsymbol{\omega}_z\dot{\theta} - \boldsymbol{d}_x\dot{\theta}^2
\end{aligned}$$

$$\begin{aligned}
\ddot{p}_y =& \boldsymbol{\alpha}_z \boldsymbol{d}_x - \boldsymbol{\alpha}_x ci\boldsymbol{d}_z + ci\ddot{\boldsymbol{p}}_y - \boldsymbol{\alpha}_y \boldsymbol{d}_z si - \ddot{\boldsymbol{p}}_x si - ci^2\boldsymbol{d}_y\boldsymbol{\omega}_x^2 - ci\boldsymbol{d}_x si\boldsymbol{\omega}_x^2 \\
& + ci^2\boldsymbol{d}_x\boldsymbol{\omega}_x\boldsymbol{\omega}_y - 2ci\boldsymbol{d}_y si\boldsymbol{\omega}_x\boldsymbol{\omega}_y - \boldsymbol{d}_x si^2\boldsymbol{\omega}_x\boldsymbol{\omega}_y + ci\boldsymbol{d}_x si\boldsymbol{\omega}_y^2 - \boldsymbol{d}_y si^2\boldsymbol{\omega}_y^2 \\
& - \boldsymbol{d}_z si\boldsymbol{\omega}_x\boldsymbol{\omega}_z + ci\boldsymbol{d}_z\boldsymbol{\omega}_y\boldsymbol{\omega}_z - \boldsymbol{d}_y\boldsymbol{\omega}_z^2 + \boldsymbol{d}_x\ddot{\theta} - 2\boldsymbol{d}_y\boldsymbol{\omega}_z\dot{\theta} - \boldsymbol{d}_y\dot{\theta}^2
\end{aligned}$$

$$\begin{aligned}
\ddot{p}_z =& -\boldsymbol{\alpha}_y ci\boldsymbol{d}_x + \boldsymbol{\alpha}_x ci\boldsymbol{d}_y + \ddot{\boldsymbol{p}}_z + \boldsymbol{\alpha}_x \boldsymbol{d}_x si + \boldsymbol{\alpha}_y \boldsymbol{d}_y si - ci^2\boldsymbol{d}_z\boldsymbol{\omega}_x^2 - \boldsymbol{d}_z si^2\boldsymbol{\omega}_x^2 \\
& - ci^2\boldsymbol{d}_z\boldsymbol{\omega}_y^2 - \boldsymbol{d}_z si^2\boldsymbol{\omega}_y^2 + ci\boldsymbol{d}_x\boldsymbol{\omega}_x\boldsymbol{\omega}_z - \boldsymbol{d}_y si\boldsymbol{\omega}_x\boldsymbol{\omega}_z + ci\boldsymbol{d}_y\boldsymbol{\omega}_y\boldsymbol{\omega}_z \\
& + \boldsymbol{d}_x si\boldsymbol{\omega}_y\boldsymbol{\omega}_z + 2ci\boldsymbol{d}_x\boldsymbol{\omega}_x\dot{\theta} - 2\boldsymbol{d}_y si\boldsymbol{\omega}_x\dot{\theta} + 2ci\boldsymbol{d}_y\boldsymbol{\omega}_y\dot{\theta} + 2\boldsymbol{d}_x si\boldsymbol{\omega}_y\dot{\theta}
\end{aligned}$$

$$H = H(\boldsymbol{\omega}, \boldsymbol{\alpha}, \ddot{\boldsymbol{p}}, \theta, \dot{\theta}, \ddot{\theta}, \boldsymbol{d})$$
$$= \begin{bmatrix} H_{11} & H_{12} & H_{13} \\ H_{21} & H_{22} & H_{23} \\ H_{31} & H_{32} & H_{33} \end{bmatrix} \tag{A.2}$$

$$\begin{aligned}
H_{11} =& \boldsymbol{\alpha}_x \boldsymbol{d}_z ci - \ddot{\boldsymbol{p}}_y ci - \boldsymbol{d}_z\boldsymbol{\omega}_y\boldsymbol{\omega}_z ci + \boldsymbol{d}_y\boldsymbol{\omega}_x^2 ci^2 - 2\boldsymbol{d}_x\boldsymbol{\omega}_x\boldsymbol{\omega}_y ci^2 - \boldsymbol{d}_y\boldsymbol{\omega}_y^2 ci^2 \\
& + \boldsymbol{\alpha}_y \boldsymbol{d}_z si + \ddot{\boldsymbol{p}}_x si + \boldsymbol{d}_z\boldsymbol{\omega}_x\boldsymbol{\omega}_z si + 2\boldsymbol{d}_x\boldsymbol{\omega}_x^2 cisi + 4\boldsymbol{d}_y\boldsymbol{\omega}_x\boldsymbol{\omega}_y cisi \\
& - 2\boldsymbol{d}_x\boldsymbol{\omega}_y^2 cisi - \boldsymbol{d}_y\boldsymbol{\omega}_x^2 si^2 + 2\boldsymbol{d}_x\boldsymbol{\omega}_x\boldsymbol{\omega}_y si^2 + \boldsymbol{d}_y\boldsymbol{\omega}_y^2 si^2
\end{aligned}$$

$$H_{12} = 2\boldsymbol{d}_x\boldsymbol{\omega}_z + 2\boldsymbol{d}_x\dot{\theta}$$
$$H_{13} = -\boldsymbol{d}_y$$

$$\begin{aligned}
H_{21} =& \boldsymbol{\alpha}_y \boldsymbol{d}_z ci + \ddot{\boldsymbol{p}}_x ci + \boldsymbol{d}_z\boldsymbol{\omega}_x\boldsymbol{\omega}_z ci + \boldsymbol{d}_x\boldsymbol{\omega}_x^2 ci^2 + 2\boldsymbol{d}_y\boldsymbol{\omega}_x\boldsymbol{\omega}_y ci^2 - \boldsymbol{d}_x\boldsymbol{\omega}_y^2 ci^2 \\
& - \boldsymbol{\alpha}_x \boldsymbol{d}_z si + \ddot{\boldsymbol{p}}_y si + \boldsymbol{d}_z\boldsymbol{\omega}_y\boldsymbol{\omega}_z si - 2\boldsymbol{d}_y\boldsymbol{\omega}_x^2 cisi + 4\boldsymbol{d}_x\boldsymbol{\omega}_x\boldsymbol{\omega}_y cisi \\
& + 2\boldsymbol{d}_y\boldsymbol{\omega}_y^2 cisi - \boldsymbol{d}_x\boldsymbol{\omega}_x^2 si^2 - 2\boldsymbol{d}_y\boldsymbol{\omega}_x\boldsymbol{\omega}_y si^2 + \boldsymbol{d}_x\boldsymbol{\omega}_y^2 si^2
\end{aligned}$$

$$H_{22} = 2\boldsymbol{d}_y\boldsymbol{\omega}_z + 2\boldsymbol{d}_y\dot{\theta}$$
$$H_{23} = \boldsymbol{d}_x$$

$$\begin{aligned}
H_{31} =& 2\dot{\theta}\boldsymbol{d}_y\boldsymbol{\omega}_x ci - \boldsymbol{\alpha}_x\boldsymbol{d}_x ci - \boldsymbol{\alpha}_y\boldsymbol{d}_y ci - 2\dot{\theta}\boldsymbol{d}_x\boldsymbol{\omega}_y ci + \boldsymbol{d}_y\boldsymbol{\omega}_x\boldsymbol{\omega}_z ci - \boldsymbol{d}_x\boldsymbol{\omega}_y\boldsymbol{\omega}_z ci \\
& - \boldsymbol{\alpha}_y\boldsymbol{d}_x si + \boldsymbol{\alpha}_x\boldsymbol{d}_y si + 2\dot{\theta}\boldsymbol{d}_x\boldsymbol{\omega}_x si + 2\dot{\theta}\boldsymbol{d}_y\boldsymbol{\omega}_y si + \boldsymbol{d}_x\boldsymbol{\omega}_x\boldsymbol{\omega}_z si + \boldsymbol{d}_y\boldsymbol{\omega}_y\boldsymbol{\omega}_z si
\end{aligned}$$

$$H_{32} = -2ci\boldsymbol{d}_x\boldsymbol{\omega}_x + 2\boldsymbol{d}_y si\boldsymbol{\omega}_x - 2ci\boldsymbol{d}_y\boldsymbol{\omega}_y - 2\boldsymbol{d}_x si\boldsymbol{\omega}_y$$
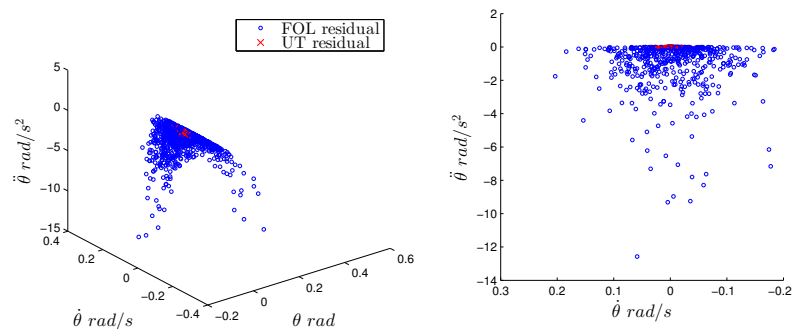$$H_{33} = 0$$

Fig. 10. The FOL causes errors in $\dot{\theta}$ and $\ddot{\theta}$ dimensions while the UT causes small errors in $\dot{\theta}$ dimension.
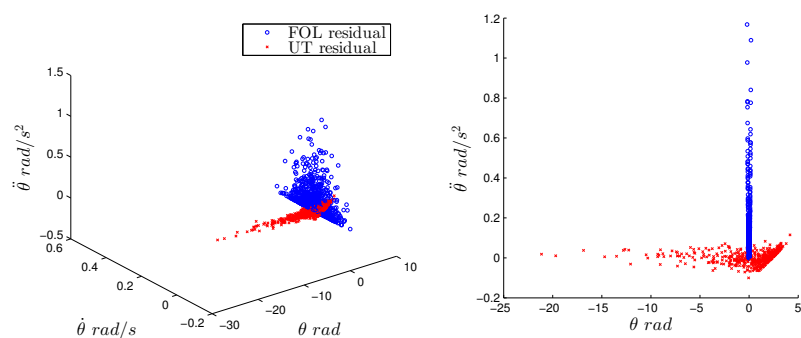

Fig. 11. The FOL causes errors in $\dot{\theta}$ and $\ddot{\theta}$ dimensions while the UT causes errors in θ dimension.
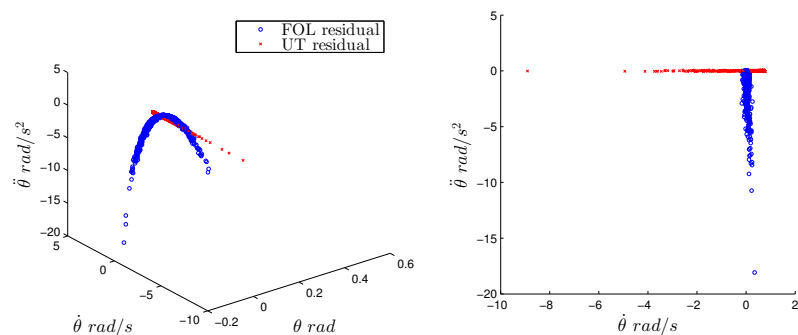

Fig. 12. The FOL causes errors in $\ddot{\theta}$ dimension and small errors in θ dimension while the UT causes errors in $\dot{\theta}$ dimension.
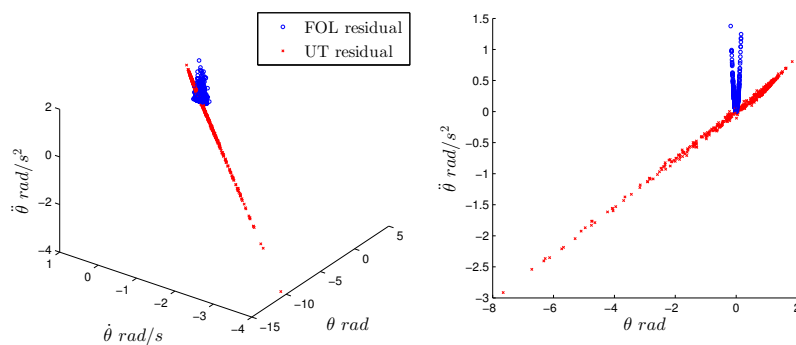

Fig. 13. The FOL causes errors in $\ddot{\theta}$ dimension and small errors in θ dimension while the UT causes errors in θ and $\ddot{\theta}$ dimensions.